

FINAL REPORT

For the period
February 28, 2001 to June 30, 2002

**EM61-3D Discrimination of UXO
Using Empirical, Analytic, and Numerical Models**

Submitted by
BLACKHAWK GEOSERVICES, INC.
301 B Commercial Rd.
Golden, CO 80401
Project 2035SER

December 24, 2002
Submitted to the
**STRATEGIC ENVIRONMENTAL
RESEARCH AND DEVELOPMENT PROGRAM**
Arlington, VA

Project CU-1215

Unclassified

Report Documentation Page			Form Approved OMB No. 0704-0188	
<p>Public reporting burden for the collection of information is estimated to average 1 hour per response, including the time for reviewing instructions, searching existing data sources, gathering and maintaining the data needed, and completing and reviewing the collection of information. Send comments regarding this burden estimate or any other aspect of this collection of information, including suggestions for reducing this burden, to Washington Headquarters Services, Directorate for Information Operations and Reports, 1215 Jefferson Davis Highway, Suite 1204, Arlington VA 22202-4302. Respondents should be aware that notwithstanding any other provision of law, no person shall be subject to a penalty for failing to comply with a collection of information if it does not display a currently valid OMB control number.</p>				
1. REPORT DATE 24 DEC 2002	2. REPORT TYPE	3. DATES COVERED 28-02-2001 to 30-06-2002		
4. TITLE AND SUBTITLE EM61-3D Discrimination of UXO Using Empirical, Analytic, and Numerical Models			5a. CONTRACT NUMBER	
			5b. GRANT NUMBER	
			5c. PROGRAM ELEMENT NUMBER	
6. AUTHOR(S)			5d. PROJECT NUMBER	
			5e. TASK NUMBER	
			5f. WORK UNIT NUMBER	
7. PERFORMING ORGANIZATION NAME(S) AND ADDRESS(ES) Blackhawk Geoservices Inc,301 B Commercial Rd,Golden,CO,80401			8. PERFORMING ORGANIZATION REPORT NUMBER	
9. SPONSORING/MONITORING AGENCY NAME(S) AND ADDRESS(ES)			10. SPONSOR/MONITOR'S ACRONYM(S)	
			11. SPONSOR/MONITOR'S REPORT NUMBER(S)	
12. DISTRIBUTION/AVAILABILITY STATEMENT Approved for public release; distribution unlimited				
13. SUPPLEMENTARY NOTES				
14. ABSTRACT				
15. SUBJECT TERMS				
16. SECURITY CLASSIFICATION OF: a. REPORT b. ABSTRACT c. THIS PAGE unclassified unclassified unclassified			17. LIMITATION OF ABSTRACT Same as Report (SAR)	18. NUMBER OF PAGES 32
				19a. NAME OF RESPONSIBLE PERSON

1. SUMMARY

The primary goal of this project was to compare three quantitative approaches to modeling EM induction for UXO discrimination: a phenomenological dipole model, a semianalytic theory, and a finite-element numerical method. The secondary goal was to quantify the value of multiple spatial components and time channels. A general, time-dependent triaxial dipole model was developed that was very successful in discrimination tests. The semianalytic theory was not completed and implementation of the numerical method was impractical given the allocated resources. The relative merits of additional temporal and spatial information were assessed by analyzing decimated data from the Geonics EM61-3D. The responses of 25 unique ordnance- and scrap-like objects buried in 45 depth-orientation states were modeled as triaxial time-dependent dipoles and were classified using the properties of the inferred model parameters. Performance was measured by the fraction of false positives for ordnance-like objects at 91% true positives. The best false-positive rate for the full multicomponent, multichannel data was just 5%, which was achieved using the power-law slope of the time decay as a discriminant: ordnance-like items remain in “intermediate” time longer and display a characteristic $-3/2$ slope, whereas scrap-like items (even those made of steel) transition to “late” time and the recovered power-law indices vary widely. However, this excellent performance is largely due to the fact that the ordnance-like objects are larger than the scrap-like objects in this data set. Better generalization may be obtained with discriminants based solely on shape—ordnance-like objects are usually axisymmetric about a long axis—which yielded 32% false positives, again in the power-law slope. In contrast, the best false-positive rate for single-component, single-channel data was 68%. Other instrument configurations (single-component, multichannel or multicomponent, single channel) were generally ranked intermediately between these extremes. This work demonstrated in an internally consistent way the high performance in UXO discrimination that can be achieved with multicomponent, multichannel electromagnetic sensors, as well as the value of relatively simple modeling and discrimination procedures.

2. INTRODUCTION

Electromagnetic (EM) induction sensors have been recognized as a principal means of UXO detection and discrimination (e.g., *Bell et al.*, 2001). Two issues regarding the use of such sensors are the kind of data acquired and the algorithms used to interpret the data. Time-domain EM (TDEM), or pulsed-induction, sensors use an abrupt change in transmitter-coil current to induce eddy currents in a target, whose decay is sensed in a receiver, usually another coil. Most such instruments use a transmitter coil in the horizontal plane. They differ in the amount and complexity of data, specifically, the number of receiver spatial components and the number, location, and width of time gates that record the eddy-current decay. Physics-based models are used to interpret these data, and three such models were studied here. A semi-empirical method treats targets as a group of infinitesimal, orthogonal, time-dependent dipoles and constructs responses for arbitrary position and orientation through linear superposition. Classification can be improved by experimentally determining the directional responses of targets of interest. The technique is very fast but is limited to distances relatively far away from the source and receiver, assumes no environmental effects, and can require prior data for each object to be classified. A semi-analytic theory is relatively fast, models the full field at arbitrary distances, and can include ground conductivity, but restricts target shapes to solid triaxial ellipsoids. Numerical models such as the finite-element method offer the most accurate solutions for arbitrary objects and environments but are slow, unsuited to parameter estimation, and require that responses from all potential targets be cataloged. The purpose of this investigation was first to assess the relative merits of these three models and second to quantify the value of increasing the amount and kind of TDEM data for UXO discrimination, providing metrics for such discrimination. Our approach focuses first on model development and second on test-plot measurements of inert ordnance, ordnance simulants, and non-ordnance.

3. MODELING

Three different modeling techniques were proposed for this work. However, an extension of the simple, widely applied dipole model proved very effective for our discrimination study while the other two reached dead ends, at least as far as we were able to pursue them here.

3.1 Mean-Field Theory

Maxwell's equations for the electromagnetic fields in a compact, conductive object can be reduced to the single equation

$$\nabla \times \left[\frac{1}{\mu} \nabla \times e^{(n)} \right] = \alpha_n \sigma e^{(n)} \quad (3.1)$$

where σ and μ are the conductivity and permeability, respectively. This is an eigenvalue problem, where the eigenvalues α_n are the mode constants and the eigenvectors $e^{(n)}$ are the electric-field shapes for mode n . This electromagnetic problem is therefore analogous to the mechanical problem of the motion of a drum head: depending on where the drum is struck, different vibrational shapes are excited. Similarly, different modes of electric-field circulation in the target will be excited depending on shape, position, and orientation with respect to the transmitter, and these fields will be sensed differently depending on the receiver configuration(s). The time-domain solution to Equation (3.1) for the electric field is

$$E(x, t) = \sum_n A_n e^{(n)}(x) \exp(-\alpha_n t) \quad (3.2)$$

where the coefficients A_n give the amplitudes of each mode.

The essence of the “Mean-Field Theory” (MFT), developed by Dr. Pieter Weichman while he was at Blackhawk Geoservices, is to find a truncated Taylor-series solution to Equation (3.2) which yields an approximation of the shape functions $e^{(n)}$ and time constants α_n . These can be

precomputed based on the target shape and the model execution speed increased by referring to these parameters in a look-up table. An actual modeling run then needs only to calculate the A_n parameters based on the source-target-receiver geometry. A triaxial ellipsoid was adopted as a canonical shape that was analytically tractable to bound the shape polymomials but flexible enough to represent diverse objects such as cylinders, discs, and spheres (**Figure 3.1**).

While elegant in principle, the MFT never reached practical application while the author was at Blackhawk. Although the lowest-order (“late-time”) constant α_l could be accurately computed and compared to analytic models, computation time and accuracy limited how well the higher-order time constants could be determined. The author was considering a one-dimensional approximation that may have provided a “patch” but would have been inconsistent with the overall approach of the model. Extension to permeable (ferrous) and hollow objects is essential for treating the UXO problem but was never within sight. After the author’s departure, we transferred development of the code to collaborator Alex Becker and his staff at UCB. This work was pursued under different funding and resulted in an order-of-magnitude improvement in the early-time accuracy of the MFT but still has not reached objects with extreme shapes or those that are steel and/or hollow. While MFT development continues externally at lower priority, we have elected to pursue other alternatives.

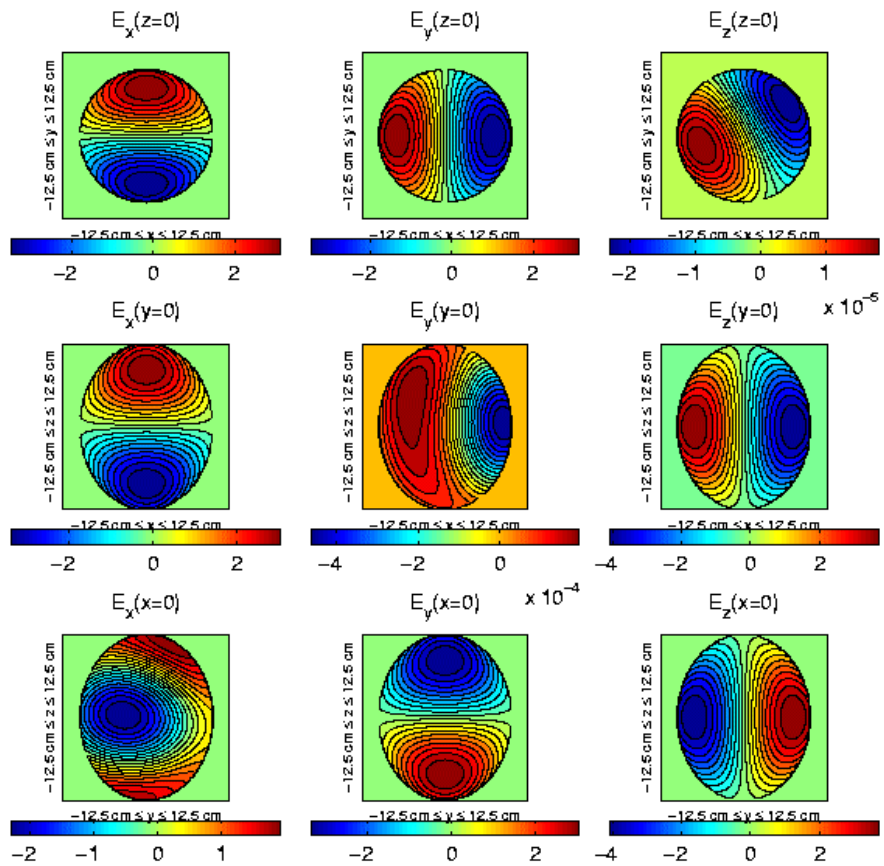


Figure 3.1 Example of fundamental ($n=1$) mode shapes for a 1.25:1:1 nonpermeable solid ellipsoid calculated using 4th order MFT.

3.2 Numerical (Finite-Element) Model

Piecewise solution of Maxwell's Equations leads to the finite-element method, which is widely used for physical analysis of complexly shaped systems. We tested the ability of the low-frequency electromagnetic module of the *ANSYS* package to solve UXO problems. The original motivation was to test and calibrate the MFT by examining the TDEM response of ellipsoids. Axisymmetric equal-volume objects with aspect ratios of 1:1 (sphere), 4:1 (prolate ellipsoid) and 1:16 (oblate ellipsoid) were modeled at 1 m directly below an EM-61 in longitudinal and transverse orientations. In the former, the axis of symmetry is vertical and in the latter the symmetry axis is horizontal. Runs were performed for both aluminum and steel targets. Aluminum objects had late-time constants α_l measured from the decay curves in good agreement with theory. Steel objects are dominated by magnetic polarizability and the rules developed for eddy currents do not apply. Instead, the magnitude of the response varies directly with the amount of steel in-line with the primary field (**Figure 3.2**).

The full capabilities of *ANSYS* were tested by constructing a geometrically accurate model of an 81-mm mortar projectile, consisting of a steel body, an aluminum fuze and tail assembly, and a “hollow” interior. The model was evaluated in nose-down and horizontal orientations beneath an EM-61. The calculations reveal the detailed structure and evolution of eddy currents (e.g., **Figure 3.3**) and magnetic induction in the target, providing substantial insight into the physics of EM sensing of UXO.

The *ANSYS* calculations provided the baseline for the MFT as required. Another objective was to be able to generate realistic “synthetic” data, saving the labor and data-reduction costs of experimental studies—this is a general goal of such modeling in industry. We found two obstacles to this. First, we discovered that working with *ANSYS* is a full-time job (perhaps well-known by the consultants on whom we relied for the early parts of this work) and we were unable to devote the resources necessary to rapidly and robustly generate target “CAD” models and finite-element meshes. Although there are many tools available in *ANSYS*, they demand a very large time investment to learn and master. Second, the cost-effectiveness trade point seemed out of reach. Model execution times are very slow (hours for a single position of the sensor with respect to the target) that several days of CPU time would likely be expended for measurements that can take as little as a few minutes for simple sensors and perhaps an hour for

a careful grid with a complex sensor. We will reserve future finite-element analysis for understanding unusual target responses that cannot be adequately modeled with simpler methods.

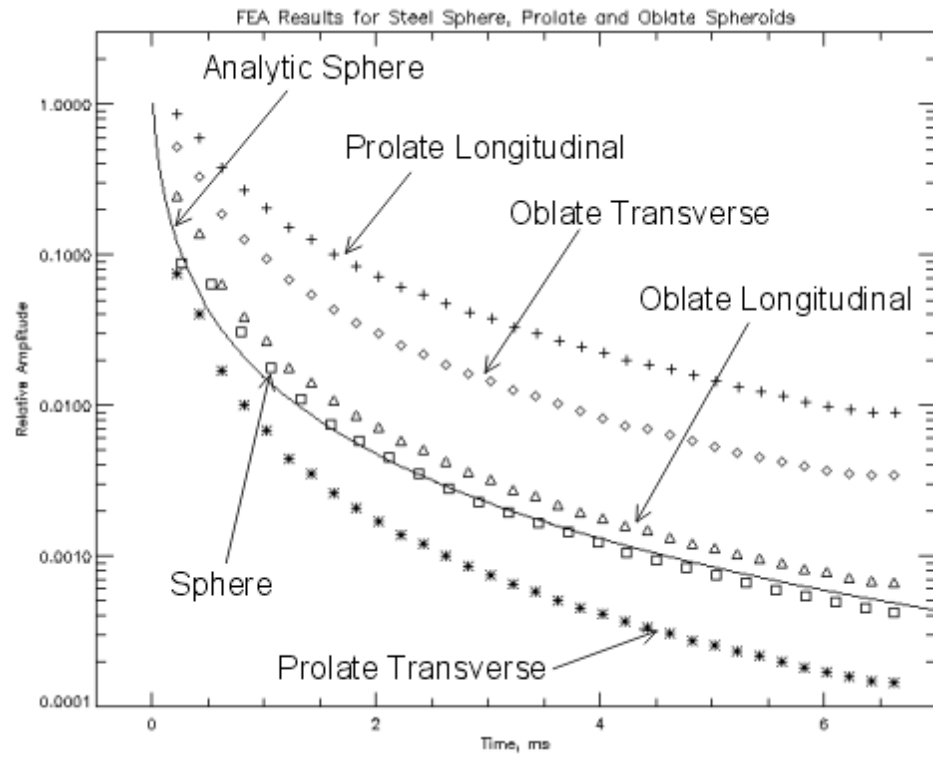


Figure 3.2. ANSYS finite-element solutions for simulated EM61 response (with expanded time scale) to steel objects. Largest response is for vertical, cylinder-like object (prolate longitudinal) because the greatest amount of steel is in line with the primary field. A plate-like object on-end (oblate transverse) similarly has a large response. Flat-lying steel plate (prolate transverse) has smallest relative response because of unfavorable orientation.

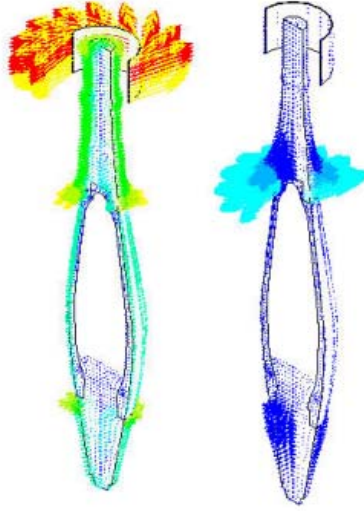


Figure 3.3. Eddy currents in 81-mm projectile at 0.6 ms (left) and 9.6 ms (right) after transmitter turn-off. Note strong early time currents in tail-fin shroud and late-time concentration in tail-boom threads. The latter occurs because currents are unable to diffuse into the steel tail-boom screw and are therefore supported to longer times than expected for a simple ring.

3.3 Dipole Model

Our dipole model extends earlier work (*McNeill and Bosnar, 1996; Barrow and Nelson, 1999, 2000; Pasion and Oldenburg, 2001; MacInnes et al., 2002*) of relatively simple models for UXO characterization. The target is treated as three orthogonal dipoles with one, two, or three independent axes (a sphere has one independent axis and an axisymmetric object has two). The incident magnetic field from a square transmitter loop (*Das et al., 1990*) is geometrically projected upon each of these axes depending on target position and orientation. The time-domain EMF V in each axis of the target is assumed to respond as

$$V = \beta(t+\delta)^{-\gamma} e^{-\alpha t} \quad (3.3)$$

where α , β , γ , and δ vary for each independent axis. The dipole secondary fields from each target axis are evaluated at the receiver to form the complete response. A spherical target measured with a single-gate system (like the EM61) requires only 4 parameters (β_1 , xyz position) whereas a fully time-dependent triaxial model requires 18 parameters (α_{123} , β_{123} , γ_{123} , δ_{123} , xyz position,

azimuth, inclination, and roll). *Grimm and Sprott* (2002) applied a triaxial model in β alone (9 parameters) to design efficient multicomponent, multiple-sensor platforms for UXO discrimination (see *Wold et al.*, 2002, for implementation). Physically the β parameters are proportional to the time derivative of the magnetic polarizability along each principal axis. The α parameters are the “late-time” exponential-decay constants, whereas the γ parameters describe the approximate power-law decay that would be represented analytically by a sum of higher-order decay constants that dominate “intermediate time.” The δ parameters, introduced by *Pasion and Oldenburg* (2001), are effectively empirical correction factors to improve the fit quality (note that these authors actually use the symbol α for this term). In contrast to the other parameters, clear patterns in the δ s could not always be discerned and in some cases the improvement in fit caused degradation in interpretation of β , α , and/or γ . The δ -parameters were therefore treated as an option and a full set of inversions was performed both with and without these parameters.

The inverse problem for target shape and orientation is solved through a generalized inverse using singular-value decomposition (e.g., *Menke*, 1984). Direct solutions for all parameters was generally not as effective as the following multi-step “recipe.”

1. Solve for the best-fitting sphere (one independent axis only) in all relevant parameters *except* δ .
2. Copy these estimates to the other axes and re-solve with 3 independent axes, including δ if desired.
3. Exchange all parameters on each axis so that the largest β value is the 1-axis and the smallest β is the 3-axis. Re-solve for orientation, holding all other parameters fixed.

The time-domain response decreases sharply with time and also varies in strength with spatial component (Z is typically larger than X or Y). In order to balance all of the data in the least-squares inversion, time- and component-equalization were implemented by normalizing each time channel and each component by its respective RMS value over all the data collected for that target. Component equalization was always applied, effectively nulling the overall Z-gain problem described above. However, this approach does not correct any intra-anomaly variations. Time equalization was treated as a free parameter; a full set of inversions was performed with and without time equalization.

4. ANALYSIS OF EM61-3D TEST-SITE DATA

4.1 Instrumentation

In geological EM exploration, the optimum approach to best describing target size, shape, and orientation is to use multiple time gates and all three spatial components of the secondary field (e.g., *Kaufman and Keller*, 1985). The Geonics EM61-3D is a multicomponent, multichannel pulsed-EM induction sensor designed to bring these capabilities to UXO discrimination (*Geonics, Ltd.*, 1996). Previous work with the EM61-3D and related prototypes are described by *McNeill and Bosnar* (1996) and *Grimm et al.* (1997). The more-recent Geonics EM63 measures a comparable time range but eliminates recording the horizontal spatial components in favor of higher signal-to-noise for the vertical component. The EM61-II also only measures the vertical component in a more restricted number of time gates. Because of numerous differences in instrument performance, the relative merits of various combinations of time gates and spatial components were assessed by progressive decimation of EM61-3D data rather than direct comparison of different instruments.

The EM61-3D consists of a 1-m diameter square transmitter coil in the horizontal plane and 3 orthogonal receiver coils averaging 0.44-m diameter (**Figure 4.1**). The Geonics PROTEM is used as a receiver. The transmitted waveform is bipolar quasi-rectangular at 50% duty. The instrument is designed to operate at repetition frequencies of 7.5 and 30 Hz; higher-quality data was obtained at the lower frequency and therefore it was used exclusively. This relatively low pulse rate, and perhaps other instrument characteristics, further required that data were acquired statically, i.e., at a series of fixed stations, rather than while moving (see *Grimm et al.*, 1997). The EMF induced in each receiver coil is recorded in 20 geometrically spaced gates spanning 0.35 to 27.9 ms for the 7.5-Hz base frequency.

The EM61-3D shows a strong time-dependent response even when there is no metallic target present. The Z-component response of worst-case conductive ground ($10 \Omega\text{-m}$) is $<2 \text{ nV/m}^2$ at 0.35 ms, the first EM61-3D time gate (TEMIX XL). However, the equivalent Blossom-Point EM61-3D data (see below) show target-free responses of 50-80 nV/m^2 . Therefore the effect must be an instrument artifact, which was approximately removed by subtracting the mean value around the periphery of each measurement grid at each time gate.

A second apparent artifact regarding the EM61-3D concerns the relative gain of the Z-component compared to X- and Y-components: the Z-component appeared to be too small in the raw data. The Z-component of the analytical response of a sphere (*Grant and West*, 1965) is a factor of ~ 3 larger than the EM61-3D response of the Blossom-Point shotput, when compared to their respective XY components. This factor was therefore applied as a gain to the EM61-3D Z-component; it must be emphasized, however, that this value is an average for measurements of just one target; it may not be constant within a target or among different targets.

4.2 Test Objects and Measurements

EM61-3D measurements were made at the test range established by the Naval Research Laboratory (NRL) at Blossom Point, MD (*Nelson et al.*, 2000). 50-cal and 20-mm projectiles and targets deeper than 0.5 m were excluded for potentially low signal-to-noise, yielding a data set consisting of 25 unique objects in 45 different states of depth and orientation (i.e., typically two instances of each object in a different depth and/or orientation). These objects included 60- and 81-mm projectiles, a Mk-23 practice bomb, a 16-lb shotput, steel cylinders and rectangular plates with different aspect ratios, and numerous clutter items (**Table 4.1**).

Each target was measured at 73 discrete stations in a nonlinear “starburst” pattern (**Figure 4.2**), that is, a radial pattern in 12 directions (30° azimuth separations) at distances of 0.15, 0.3, 0.5, 0.85, 1.5, and 2.7 m, in addition to (0,0). This pattern allowed recovery of detailed anomaly shapes over the target but also included low-resolution mapping on the periphery of the anomaly. Debiasing and gain corrections were applied as discussed above.

4.3 Classification

UXO discrimination or classification has proved to be more effective upon model-derived parameters rather than the geometry or energy of the geophysical anomaly itself (*Hart et al.*, 2000; *Collins et al.*, 2001). Here the intrinsic parameters derived from the dipole model (those that are properties of the target itself) are used and the extrinsic parameters (derived position and orientation) are disregarded. Direct discrimination upon all of the intrinsic parameters of the time-dependent triaxial dipole is a 12-dimensional problem: although classifiers may perform

well on a training data such as that used here, generalization to new data can be poor because the classifier is making direct comparisons against many individual parameters for each training example. Two approaches to reducing the parameter space are nondimensionalization and selection of more specific discrimination metrics derived from the individual model parameters.

Nondimensionalization is implemented by dividing each parameter by a reference value. Recall that the polarizability derivatives were defined above so $\beta_1 \geq \beta_2 \geq \beta_3$; adopting the 1-axis as the reference, the three β s are expressed as two parameters $\beta_3/\beta_1 \leq \beta_2/\beta_1 \leq 1$. Other parameters are expressed similarly with respect to the 1-axis, although there are no inequality constraints. This nondimensionalization now implies that classification will be more weighted by shape—a relative measure—and less by the model parameters themselves, which indicate both shape and absolute size. Although there may be less difference between, say, 40-mm and 155-mm projectiles using these metrics, the goal is to achieve better discrimination of long, axisymmetric objects relative to more irregularly shaped scrap, regardless of size.

Indeed, near-axisymmetry is a defining shape characteristic of most ordnance and is adopted in a weak and strong form in two classification algorithms. The weak form classifies objects by their axisymmetry but then simply measures how well the shape factors above are grouped by class. The strong form uses the same classification but explicitly measures the axisymmetry of the object by the normalized difference in shape factors, e.g.,

$$\beta_{\text{axi}} = 1 - |\beta_2/\beta_1 - \beta_3/\beta_1| / (\beta_2/\beta_1 + \beta_3/\beta_1) \quad (4.1)$$

and similarly for other parameters as desired. This is an implementation of the second approach above to parameter-space reduction. The minimum value of the axisymmetry is 0 (when either of the 2- or 3-axes is zero) and the maximum is 1 (when the values for the 2- and 3-axes are equal).

The Blossom-Point test objects were classified as “ordnance-like” where axisymmetric about a long axis, i.e., roughly cylindrical or spherical shapes. The 10 distinct ordnance-like objects consisted of the steel cylinders, projectiles, practice bomb, and shotput. The presence of tail fins that formally break true axisymmetry was disregarded. These ordnance-like objects were measured in a total of 23 depth-orientation states. Other items that were triaxial or axisymmetric about a short axis were classified as “scrap-like.” The 15 scrap-like objects consisted of the

rectangular steel plates and clutter items described above and were measured in a total of 22 depth-orientation states.

The weak form of the axisymmetry discriminator was implemented by a generalized regression neural network (GRNN; *Wasserman*, 1993). This is a radial basis-function method that requires no iterative training and approximates any arbitrary function between input and output vectors. The input vectors consist of up to 8 shape factors described above (2 for each of the 4 parameter groups in Eqn. 3.3). As a classifier, the output vectors are taken to be the class probabilities and the GRNN approximates a probabilistic neural network (PNN; *Wasserman*, 1993; *Hart et al.*, 2000). In a two-class system, the PNN output vectors provided for training are usually taken as 0 or 1; for the GRNN nonzero values are preferred numerically, so the target outputs are assigned 1 or 2. The simplest GRNN or PNN has a single free parameter σ which is the standard deviation of the gaussian basis function or kernel. When σ is small, the GRNN extrapolates and the PNN classifies based on the nearest neighbor in the set of input vectors. When σ is large, the PNN approximates a Bayesian classifier (i.e., it yields the mode of the training values) but GRNN produces the (nonintegral) mean of the training values. The network performance is assessed using leave-one-out cross training. In this algorithm, the network is asked to predict the output vector at one withheld data point. Now the test datum could be most simply classified according to its rounded output vector (e.g., >1.5 is predicted ordnance-like for the GRNN) but in practice a series of thresholds is tested. At each threshold, the fraction of correctly classified ordnance (true positives) is designated the Probability of Detection (PD) and the fraction of scrap incorrectly classified as ordnance (false positives) is designated the Probability of False Alarm (PFA). The ensemble of PFA vs. PD as a function of output threshold is the Receiver Operating Characteristic (ROC) curve.

The strong form of axisymmetry discrimination uses a straightforward cutoff in the axisymmetry metric (Eqn. 4.1). Therefore the strong cutoff discriminator uses “hard” weights whereas the weak GRNN discriminator uses “soft” weights. The strong-form algorithm allows different parameters to use different cutoffs such that the cutoff surface is ellipsoidal, i.e.,

$$R = \sum_i [(1-A_i)/(1-c_i)]^2 \quad (4.2)$$

where R is the normalized distance from 100% axisymmetry for a test datum ($R < 1$ is classified as ordnance), A_i is the i^{th} of up to 4 axisymmetry measures for that datum (e.g., β_{axi}) and $0 < c_i < 1$ is the cutoff value for the i^{th} parameter. The cutoff is swept independently for each of the parameters; the fraction of ordnance and the fraction of scrap for each multiparameter cutoff value at $R < 1$ are accumulated into PD and PFA, respectively, and a sort is subsequently required to order PD and PFA for a ROC curve.

4.4 Results

4.4.1 Sample Parameter Inversion

Sample results are shown in **Figures 4.3-4.6** and **Table 4.2**. The target is a 3" diameter by 12" long stainless steel cylinder buried at 0.5-m below ground surface, lying horizontally and pointing to magnetic north. The EM61-3D data were interpolated to a regular grid for display but analysis is performed on the raw data. Note the distinct character of the X, Y, and Z spatial components. The sample inversion (Table 4.2) used the full data set under spatial and temporal equalization and included the δ parameters. The overall goodness-of-fit is 96%. The β and γ parameters for the minor axes are 79% and 99% axisymmetric (Eqn. 4.1), respectively, but the α and δ parameters for the minor axes are 0% and 43% axisymmetry, respectively. The zero value of axisymmetry in α follows from a zero value in a minor axis, which in turn was an explicit movement and not a lack of change from initialization. The ratio of the major β to the geometric mean of the minor values is 3.4:1, which somewhat underestimates both the aspect ratio of the cylinder (4:1) and the DC polarizability ratio (5.8:1) for a magnetically permeable ellipsoid with similar dimensions to the cylinder (Das *et al.*, 1990). Recall, however, that the β s are time derivatives of the polarizability and are also dimensionally influenced by values of γ . The recovered position and orientation are in excellent agreement with the true values; the largest discrepancy is depth, which is too large by 0.14 m or 16% of the sensor-target distance.

4.4.2 General Solutions

Several inversions were performed for each of the 45 buried targets, switching by system, parameterization, and equalization. In the first, EM61-3D data were decimated to emulate systems acquiring less spatial and/or temporal data. The systems were denoted as follows:

A – Z-component receiver, single time gate centered at 0.6 ms (EM61 simulant).

B – XYZ receiver, single time gate.

C – Z receiver, 20 time gates (EM63 simulant).

D – XYZ receiver, 20 time gates (full EM61-3D).

E – XY receiver, 1 time gate.

F – XY receiver, 20 time gates.

The second and third switches were whether or not the δ parameter and temporal equalization were selected. In all, these variations led to 675 individual inversions.

Results are grouped by instrument configuration and discrimination approach (**Table 4.3**). The column headings are configuration given above. The row headings describe the model parameters and specific method used for discrimination. “Ratios” and “LogRatios” indicate the weak-form (GRNN) discrimination, whereas “Axisymm” denotes the strong-form (axisymmetry cutoff) discrimination. The average PFA over all inversions at 91% PD is reported as the principal measure of discrimination performance (This PD corresponds to 21/23 correctly classified ordnance-like objects). Configurations A, B, and E cannot estimate the temporal parameters α , γ , or δ and so these entries are blank. Good performance (highlighted as PFA < 50%) largely lies within configurations D and F, i.e., the systems with multiple time channels recording at least the X and Y field components.

The value of δ and time equalization were assessed by the average changes in PFA at PD = 91% by alternately incorporating and neglecting these factors. As both deal with temporal effects, they apply only to the multichannel configurations C, D, and F. The parameter δ results in a small but quantifiable improvement in discrimination (**Table 4.4**), whereas time equalization yields a major increase in discrimination ability (**Table 4.5**) because the temporal parameters are better estimated. Note that these conclusions are based on typical changes; individual cases can be adversely affected.

4.4.3 Discrimination Using the Power-Law Slope

The final results (**Table 4.6**) incorporate both δ and time equalization. The median goodness of fit is 93%, with no difference between ordnance- and scrap-like items. Very good discrimination performance ($PFA < 25\%$ at 91% PD) is highlighted. The best classification (5% PFA at 91% PD) was achieved using the full EM61-3D multicomponent multichannel data and analyzing the ratios of γ alone (Table 6, “ γ -Ratios”). The optimum value of the GRNN normalized standard deviation σ is 0.7, indicating that the neural-network weighting spans a significant portion of the parameter space and therefore should be somewhat generalizable. The quality of the classification is intuitively obvious from the tight grouping in the γ ratios of ordnance-like objects (**Figure 4.7**). This grouping implies values just greater than unity for all three γ , which is shown in expanded form in **Figure 4.8a**. The geometric mean of the three values $\langle \gamma \rangle$ (Figure 4.8b) emphasizes the relatively narrow range (1-2) of this parameter for ordnance-like objects. There is much more variability in γ among scrap-like items in both of these plots. By simply selecting $\langle \gamma \rangle = 1-2$ in Figure 4.8b, $PD = 100\%$, $PFA = 39\%$ is realized.

The close clustering of γ for ordnance-like objects is due to their ability to sustain diagnostic eddy currents longer than scrap-like objects. *McNeill and Bosnar* (1996) describe the different stages of time-domain electromagnetic induction in a compact permeable conductor. “Early time,” just after transmitter turn-off, is characterized by a near-constant magnetic field in the target that is established by surface eddy currents as a consequence of Faraday’s Law. As eddy currents diffuse into the object’s interior the magnetic field decays as $t^{-1/2}$; this is “intermediate time.” Finally, eddy currents penetrate the entire body during “late time,” which is characterized by an exponential decay of the magnetic field. When EMF is the measured quantity, voltage decays as $t^{-3/2}$ during intermediate time. The beginning and end of intermediate time are determined by the size and shape of the object, but the power-law slope of the EMF during intermediate time is always $-3/2$. The observed range of γ between 1 and 2 for the ordnance-like items is in excellent agreement with theory. As an object transitions to late time, the recovered value of γ should in principle approach 0, but in practice a wide range can be inferred due to ambiguity in the curve fitting. This is exactly what is observed for the scrap-like objects.

Pasion and Oldenburg (2001) suggested that a mean γ (which they call β) in excess of 0.8 for axisymmetric objects is diagnostic of magnetically permeable materials. They calculated the effect of variable permeability upon spheres of different sizes, but the smallest sphere they considered had a volume of $\sim 500 \text{ cm}^3$. This is approximately the median volume of the ordnance-like objects analyzed here, but the scrap-like objects have a median volume of $\sim 100 \text{ cm}^3$. Only three of the scrap-like items are nonferrous. Therefore the result of *Pasion and Oldenburg* (2001) should be generalized to state that magnetically permeable objects show γ in the specific range 1-2 when the object is sufficiently large to sustain early-to-intermediate time currents through the recorded time range. Nonpermeable or smaller permeable objects show widely varying γ indicating that the power-law slope was not accurately recovered.

The comparatively large size discrepancy between the ordnance-like and scrap-like items analyzed here (Figure 4.8c) implies that the demonstrated clear discrimination in γ is not due to shape under the weak-form axisymmetry but to size. While this in itself is a powerful and useful result, a discriminant is still desired where the ordnance and scrap are comparable in size. The strong form of axisymmetry can be so applied, as it effectively measures the distance to the diagonal in each panel of Figure 4.7 without regard to clustering. **Figure 4.9** shows that the axisymmetry separation for ordnance-like vs. scrap-like objects is very good in γ , good in β , and poor in α and δ . The classification ability in γ alone (Table 4.6, “ γ -Axisymm”) is PFA = 32% at PD = 91%. This measure should provide greater generalization to new data.

4.4.4 Ranking of Configurations

The mean values within each column in Table 6 can be used to assign the following overall ranking to the different configurations:

- 1 – XYZ components, multiple time channels (D)
- 2 – XY components, multiple time channels (F)
- 3 – XYZ components, single time channel (B)
- 4 – Z component, multiple time channels (C)
- 5 – Z component, single time channels (A)
- 6 – XY components, single time channel (E)

An alternative metric that used the four best overall discriminators for the multichannel configurations ($\beta\alpha\gamma$ log ratios, $\beta\gamma$ log ratios, γ log ratios, γ ratios) yielded the same ranking.

The full multicomponent, multichannel data set clearly provides the best overall discrimination. Multichannel XY was the second best and much better than multichannel Z; indeed, single-channel XYZ outperformed the latter. However, single-channel XY was the worst-performing configuration. The details of these rankings may lie in the overall quality of the EM61-3D data, in the limited number and variability of test targets, or in the applicability of the dipole model or granularity in the inversion procedures. What is clear is that there is a large decrease in performance from the XYZ and XY multichannel configurations to all others, especially when the four best discrimination schemes are selected. Therefore both multiple spatial components and multiple time gates must be measured for optimal UXO discrimination. Complete ROC curves for the two best GRNN discriminators and the best strong-form axisymmetry classifier are compared to GRNN results for a single-component, single-channel system in **Figure 4.10**. Improvements at 91% PD are 40-60%.



Figure 4.1. Geonics EM61-3D at field test site. Horizontal, square transmitter coil contains three orthogonal, circular receiver coils. Transmitter and receiver electronics are to left.



Figure 4.2. Nonlinear grid used for both high spatial resolution near target center and complete coverage distant from target. See text for details.

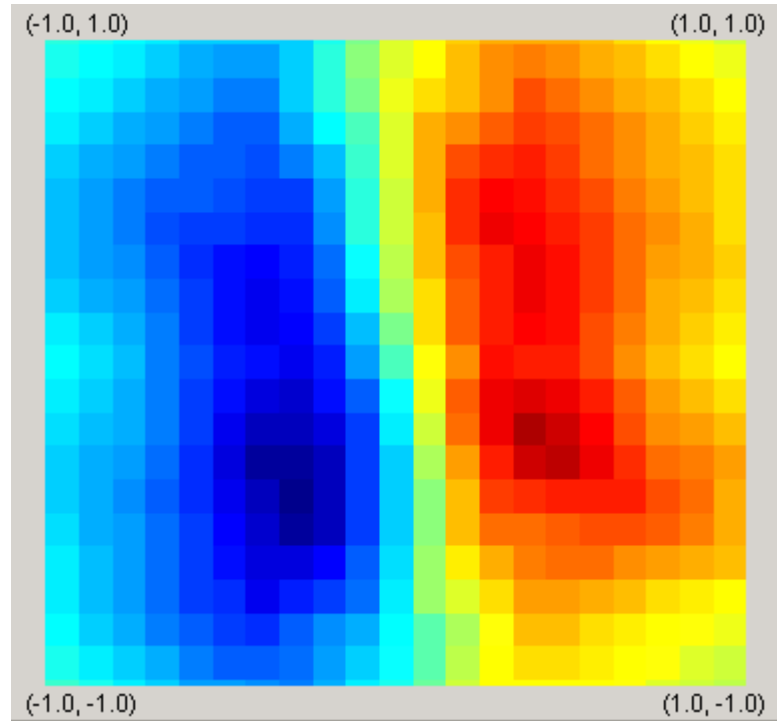


Figure 4.3. Interpolated map view of the X-component of the EM61-3D response in time gate 5 (0.8 ms) for a horizontal, 3"x12" steel cylinder buried at 0.5-m depth. Grid is oriented true north but target points magnetic north. Full color scale (blue to red) is -5 to $+5$ nV/m 2 .

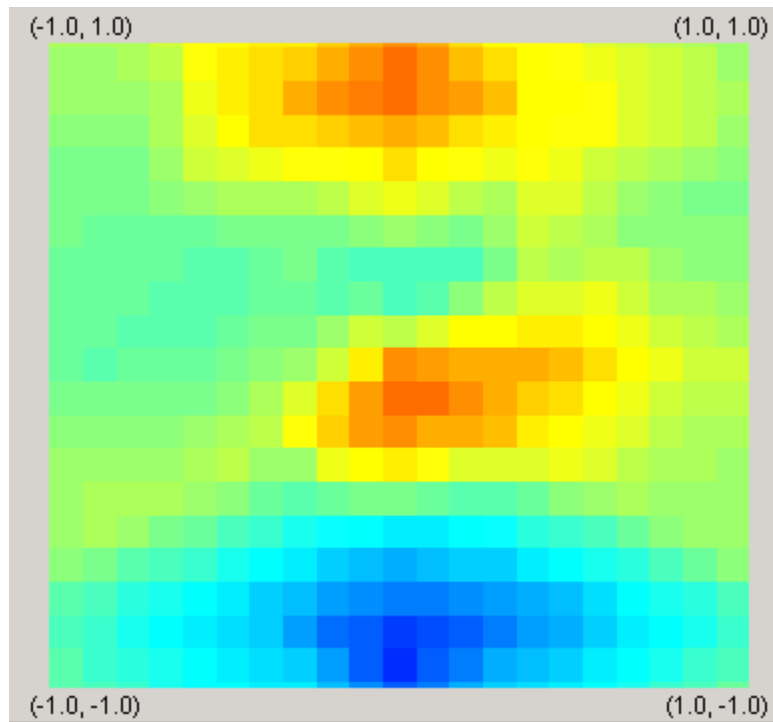


Figure 4.4. As Figure 4.3, Y-component, same color scale -5 to $+5$ nV/m 2 .

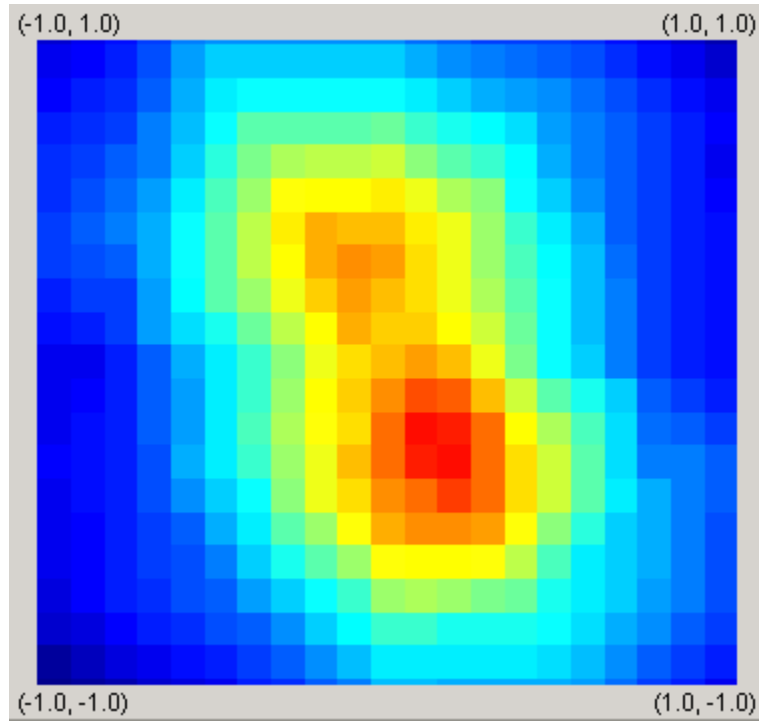


Figure 4.5. As Figure 4.3, Z-component. Full color scale is 0 to 20 nV/m².

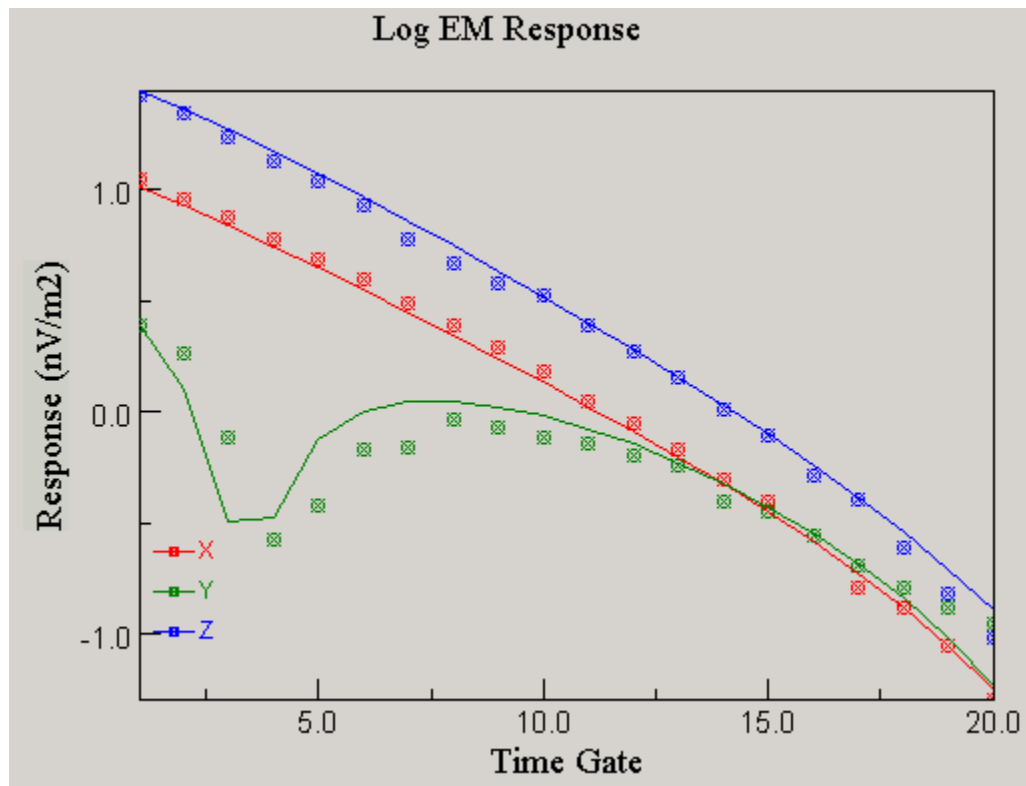


Figure 4.6. Temporal response of target in previous figures, evaluated at $x = y = -0.25$ m. Log scale; notch in Y-component response is sign reversal.

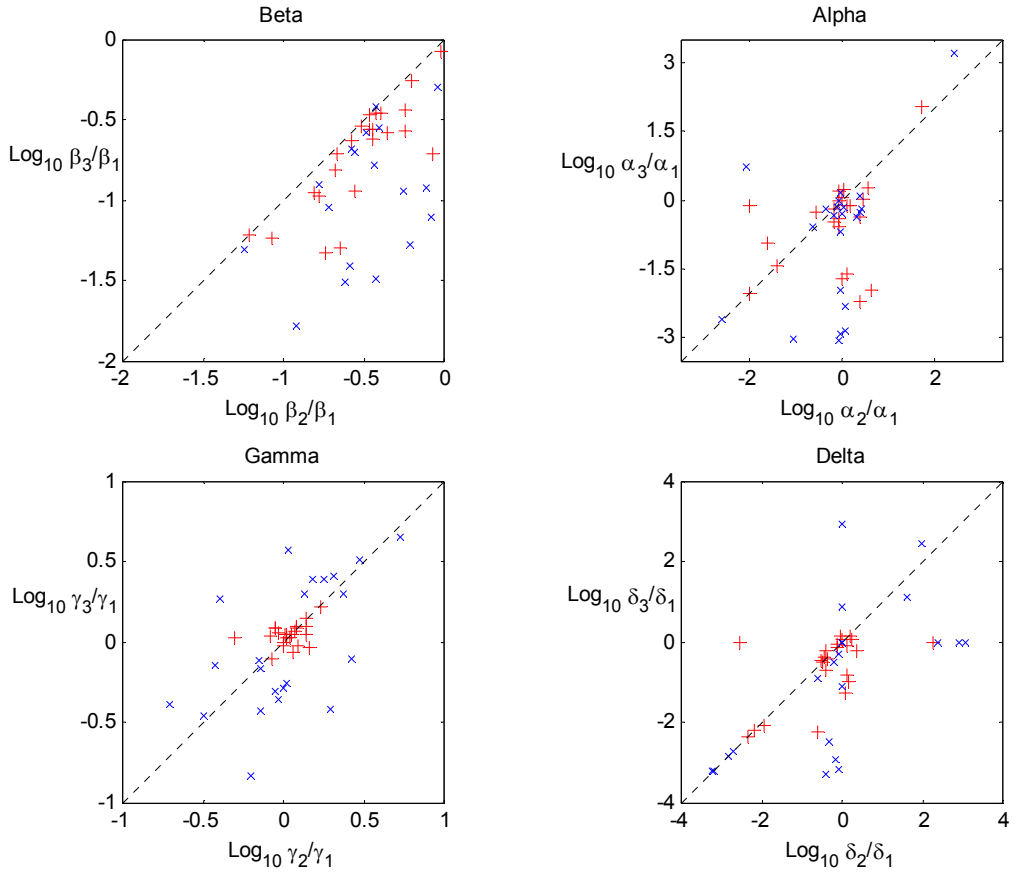


Figure 4.7. Dimensionless minor-axis model parameters for full EM61-3D data (configuration D) including both δ parameter and time equalization. Ordnance-like objects are red crosses and scrap-like objects are blue x's. Four scrap objects lie outside the plotted β ranges. Note good separation of ordnance and scrap in β and excellent separation in γ .

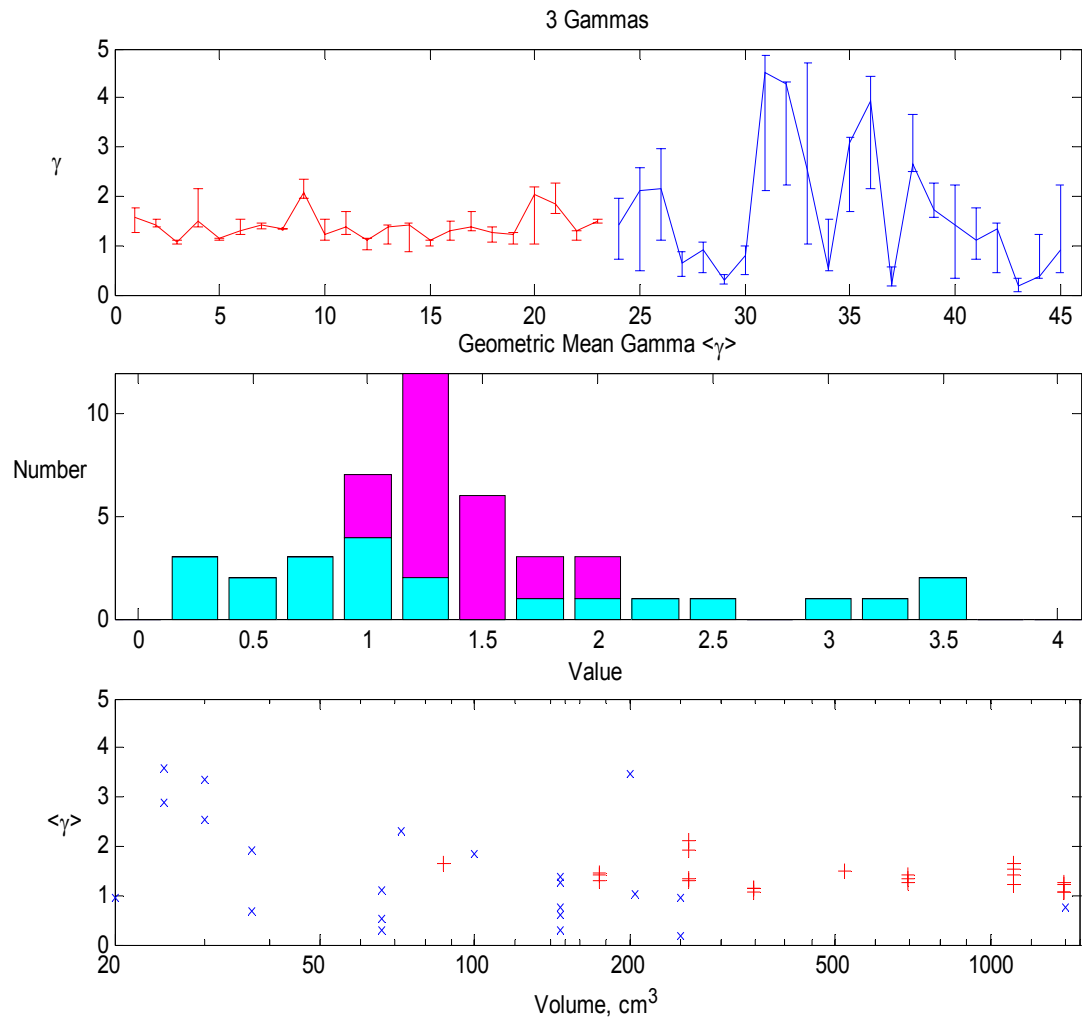


Figure 4.8. Discrimination of ordnance-like objects using power-law slope (γ) of TDEM decay. *A*: breakout of minimum, intermediate, and maximum γ -values for ordnance-like (numbers 1-23, red) and scrap-like (numbers 24-45, blue) targets. *B*: Geometric mean of 3 γ -values $\langle\gamma\rangle$ for ordnance-like (magenta, dark) and scrap-like (cyan, light) objects. $\langle\gamma\rangle$ lies in range 1-2 for ordnance-like objects. *C*: $\langle\gamma\rangle$ vs. object volume for ordnance-like (red crosses) and scrap-like (blue x's) objects. Correlation of $\langle\gamma\rangle$ with target type is largely due to size in this data set.

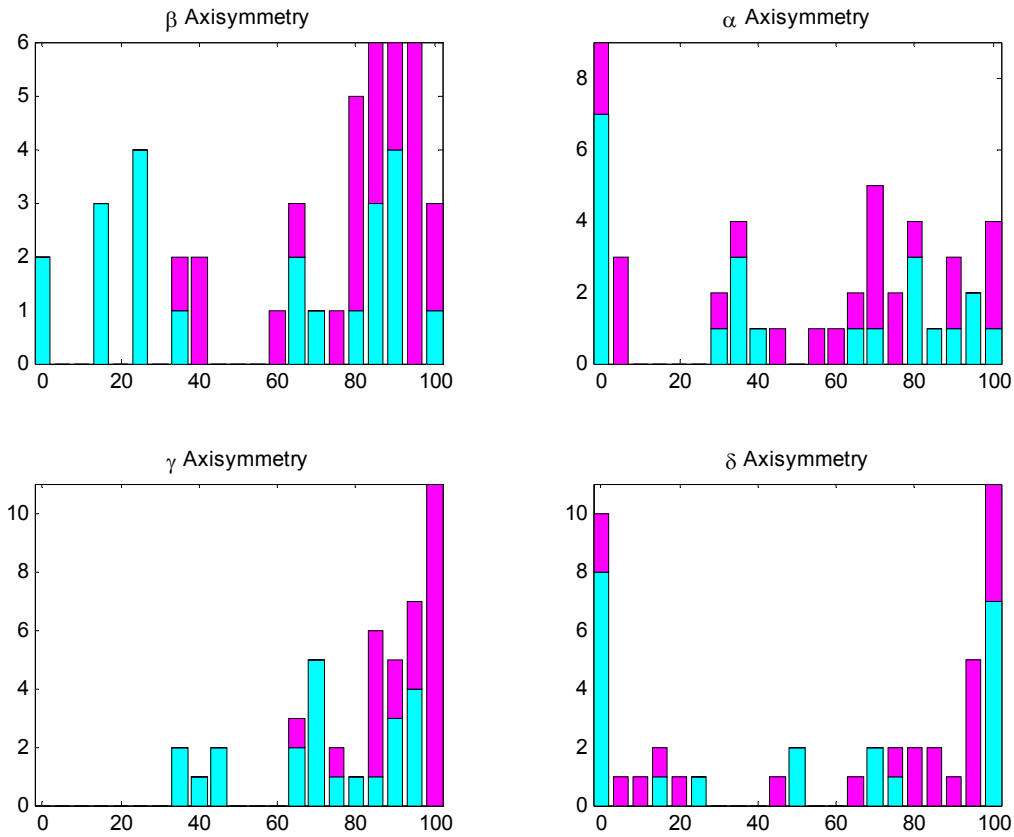


Figure 4.9. Histograms of minor-axis model-parameter axisymmetry for full EM61-3D data (configuration D) including both δ parameter and time equalization. Ordnance-like objects are magenta (dark) and scrap-like objects are cyan (light). Note very good axisymmetry separation in γ , good separation in β , and poor separation in α and δ . Higher axisymmetry is effectively a shorter perpendicular distance to the dotted diagonals in Figure 4.7. Cutoffs in multiparameter axisymmetry form basis of “strong” discrimination method.

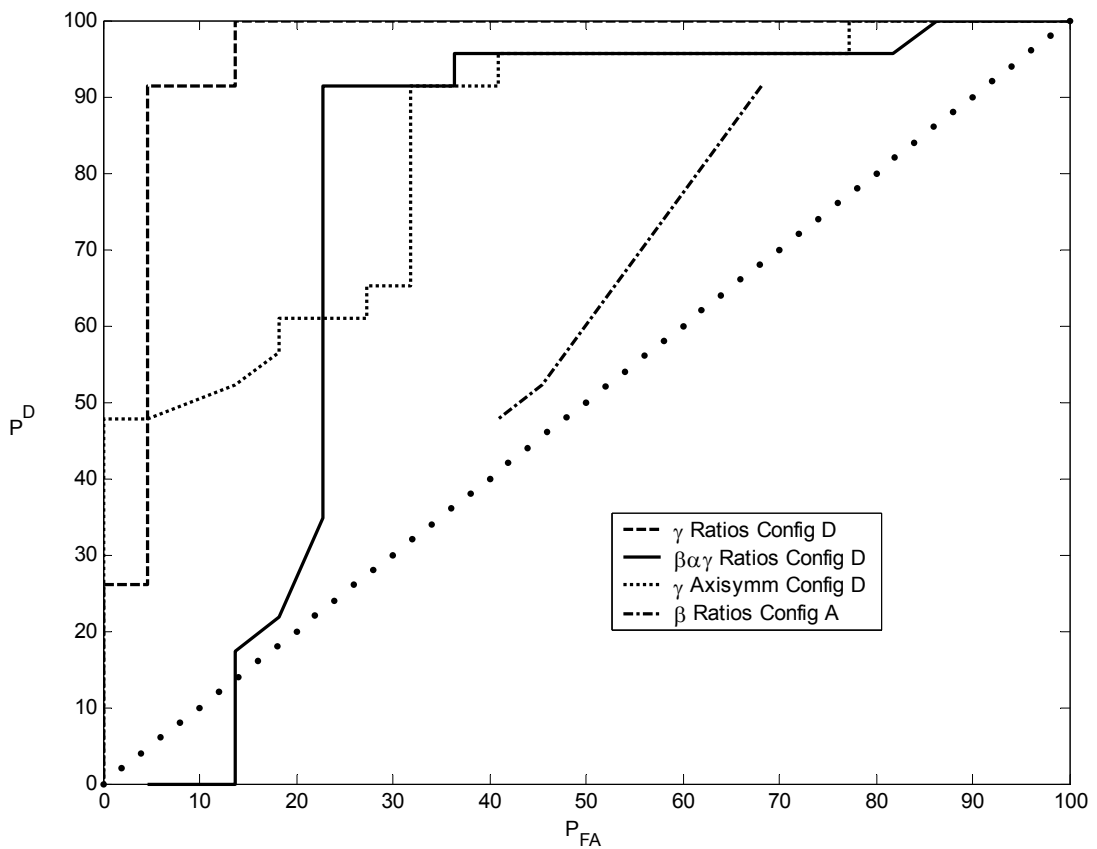


Figure 4.10. Receiver Operating Characteristic (ROC) curves for selected instrument configurations and discrimination approaches. “Weak” form discrimination for γ ratios has excellent performance but is likely not sufficiently general. “Strong” form discrimination in γ axisymmetry is very good and is likely to lead to better generalization.

Table 4.1. Modeled Test-Range Objects

Nr.	Description	Depth, m	Azimuth, deg	Inclination, deg	Nr.	Description	Depth, m	Azimuth, deg	Inclination, deg
<i>ORDNANCE-LIKE</i>					<i>SCRAP-LIKE</i>				
1	81-mm proj.	0.35	0	0	24	12"x3"x ¹ / ₄ " plate	0.15	0	0
2	6"x1.5" cyl.	0.1	0	90	25	12"x3"x ¹ / ₄ " plate	0.25	0	0
3	12"x1.5" cyl.	0.5	0	90	26	6"x1.5"x ¹ / ₄ " plate	0.05	90	0
4	81-mm proj.	0.5	0	0	27	12"x3"x ¹ / ₄ " plate	0.15	0	90
5	12"x1.5" cyl.	0.35	0	0	28	12"x3"x ¹ / ₄ " plate	0.25	90	0
6	Mk-23 bomb	0.25	0	0	29	12"x3"x ¹ / ₄ " plate	0.15	90	0
7	6"x3" cyl.	0.1	0	0	30	6"x1.5"x ¹ / ₄ " plate	0.08	0	90
8	6"x3" cyl.	0.1	0	90	31	box fin	0.35	0	0
9	Mk-23 bomb	0.25	0	90	32	shovel blade	0.23	0	0
10	Mk-23 bomb	0.15	0	0	33	flat soda can (Al)	0.03	0	0
11	81-mm proj.	0.5	0	90	34	twisted steel	0.23	0	0
12	12"x3" cyl.	0.35	0	90	35	banding wire	0.1	0	0
13	12"x3" cyl.	0.35	0	0	36	barbed wire	0.1	0	0
14	12"x3" cyl.	0.5	0	0	37	4"x4"x ¹ / ₄ " Al plate	0.05	0	0
15	12"x3" cyl.	0.5	0	90	38	box fin	0.1	0	0
16	6"x1.5" cyl.	0.2	0	0	39	rocket fins	0.1	0	0
17	6"x1.5" cyl.	0.2	0	90	40	8" round steel plate	0.15	0	0
18	81-mm proj.	0.35	0	90	41	2"x8"x ¹ / ₄ " Al plate	0.05	0	0
19	12"x1.5" cyl.	0.35	0	90	42	fence-post cap	0.08	0	0
20	3"x1.5" cyl.	0.05	0	0	43	8"x8"x ¹ / ₄ " plate	0.25	90	90
21	Mk-23 bomb	0.15	0	90	44	4"x4"x ¹ / ₄ " plate	0.05	90	90
22	6"x3" cyl.	0.25	0	0	45	8"x8"x ¹ / ₄ " plate	0.25	135	90
23	16-lb shotput	0.25	-	-					

Azimuth and inclination are with respect to longest target axis. Azimuth measured east from north, inclination up from horizontal.

Table 4.2. Model Solution for 3"x12" Steel Cylinder

$\beta_1 = 21,000$	$\beta_2 = 7600$	$\beta_3 = 5000$
$\alpha_1 = 0.042$	$\alpha_2 = 0.0$	$\alpha_3 = 0.005$
$\gamma_1 = 0.85$	$\gamma_2 = 1.46$	$\gamma_3 = 1.42$
$\delta_1 = 0.14$	$\delta_2 = 0.31$	$\delta_3 = 0.085$
$x = 0.02$	$y = 0.01$	$z = 0.64$
$az = 172$	$inc = 4$	$roll = 12$

Known values are $x = y = 0$; $z = 0.5$, $az = 0$ (or 180), $inc = 0$, $roll = \text{arbitrary}$.

Units are $\beta - \text{nV-ms}^{\gamma}/\text{m}^2$; $\alpha - \text{ms}^{-1}$; $\gamma - \text{dimensionless}$; $\delta - \text{ms}$; $x, y, z - \text{m}$; $az, inc, roll - \text{degrees}$; angles measured with respect to β_1 -axis.

Table 4.3. PFA @ PD = 91% — Average Over All Results

Discrimination	Configuration					
	A	B	C	D	E	F
β -Axisymm	82	46	73	45	96	49
β -Ratios	68	73	69	72	91	67
β -LogRatios	86	64	80	64	77	56
γ -Axisymm	---	---	83	68	---	66
γ -Ratios	---	---	66	43	---	51
γ -LogRatios	---	---	69	44	---	44
$\beta\alpha$ -Axisymm	---	---	82	56	---	67
$\beta\alpha$ -Ratios	---	---	65	69	---	66
$\beta\alpha$ -LogRatios	---	---	80	60	---	53
$\beta\gamma$ -Axisymm	---	---	81	48	---	48
$\beta\gamma$ -Ratios	---	---	63	49	---	47
$\beta\gamma$ -LogRatios	---	---	66	41	---	32
$\beta\alpha\gamma$ -Axisymm	---	---	82	58	---	59
β -Axisymm	---	---	63	44	---	47
β -Ratios	---	---	61	47	---	42

“Axisymm” is “strong” form discrimination; “Ratios” and “LogRatios” are “weak” forms.
Good performance (<50% PFA) is highlighted.

Table 4.4. Average PFA Differentials Due to Delta Parameter

Solution	Configuration					
	A	B	C	D	E	F
β -Axisymm	---	---	23	5	---	-7
β -Ratios	---	---	-7	-21	---	2
β -LogRatios	---	---	-18	-18	---	-7
γ -Axisymm	---	---	-11	-18	---	-23
γ -Ratios	---	---	-5	9	---	2
γ -LogRatios	---	---	-16	7	---	2
$\beta\alpha$ -Axisymm	---	---	18	-16	---	-25
$\beta\alpha$ -Ratios	---	---	7	-16	---	-5
$\beta\alpha$ -LogRatios	---	---	18	-16	---	-2
$\beta\gamma$ -Axisymm	---	---	-7	-5	---	-14
$\beta\gamma$ -Ratios	---	---	-2	-16	---	-7
$\beta\gamma$ -LogRatios	---	---	0	-14	---	-14
$\beta\alpha\gamma$ -Axisymm	---	---	18	-11	---	-18
$\beta\alpha\gamma$ -Ratios	---	---	7	-2	---	-2
$\beta\alpha\gamma$ -LogRatios	---	---	-14	-16	---	-16

Median changes to configurations C, D, and E are -2, -16, and -7, respectively.

Other configurations cannot model temporal parameters and therefore are not applicable.

Table 4.5. Average PFA Differentials Due to Time Equalization

Solution	Configuration					
	A	B	C	D	E	F
β -Axisymm	---	---	-27	0	---	20
β -Ratios	---	---	-20	-7	---	-7
β -LogRatios	---	---	-11	-5	---	-25
γ -Axisymm	---	---	-16	-46	---	-14
γ -Ratios	---	---	-39	-50	---	-48
γ -LogRatios	---	---	-36	-43	---	-43
$\beta\alpha$ -Axisymm	---	---	0	18	---	23
$\beta\alpha$ -Ratios	---	---	-32	-16	---	0
$\beta\alpha$ -LogRatios	---	---	-25	-7	---	-30
$\beta\gamma$ -Axisymm	---	---	-18	0	---	5
$\beta\gamma$ -Ratios	---	---	-25	-30	---	-25
$\beta\gamma$ -LogRatios	---	---	-43	-27	---	-32
$\beta\alpha\gamma$ -Axisymm	---	---	0	9	---	41
$\beta\alpha\gamma$ -Ratios	---	---	-34	-43	---	-25
$\beta\alpha\gamma$ -LogRatios	---	---	-48	-30	---	-43

Median changes to configurations C, D, and E are -25, -16, and -25, respectively.

Other configurations cannot model temporal parameters and therefore are not applicable.

Table 4.6. PFA @ PD = 91%. Final Results Using Delta Parameter and Time Equalization.

Solution	Configuration					
	A	B	C	D	E	F
β -Axisymm	82	46	86	55	96	55
β -Ratios	68	73	77	59	91	77
β -LogRatios	86	64	77	50	77	46
γ -Axisymm	---	---	100	32	---	55
γ -Ratios	---	---	64	5	---	27
γ -LogRatios	---	---	68	9	---	23
$\beta\alpha$ -Axisymm	---	---	100	100	---	100
$\beta\alpha$ -Ratios	---	---	64	55	---	68
$\beta\alpha$ -LogRatios	---	---	77	59	---	46
$\beta\gamma$ -Axisymm	---	---	68	50	---	41
$\beta\gamma$ -Ratios	---	---	73	23	---	46
$\beta\gamma$ -LogRatios	---	---	77	9	---	23
$\beta\alpha\gamma$ -Axisymm	---	---	100	100	---	100
$\beta\alpha\gamma$ -Ratios	---	---	64	23	---	46
$\beta\alpha\gamma$ -LogRatios	---	---	46	23	---	18

High performance (<25% PFA) is highlighted. 100% PFA indicates ROC curve did not achieve 91% PD.

5. CONCLUSIONS

Of the three physics-based models investigated, only the simplest—the dipole—is presently suitable for UXO studies. We extended this model from the triaxial, time-independent model of *Barrow and Nelson* (2001) and the axisymmetric, time-dependent model of *Pasion and Oldenburg* (2001) to a full triaxial, time-dependent representation. This model was used to infer target properties using multicomponent, multichannel time-domain electromagnetic signatures of 45 seeded objects were obtained using the Geonics EM61-3D. Instrument limitations required static data acquisition; a nonlinear grid was used to assure both high spatial density directly over the targets and adequately broad coverage. Neither of these constraints is applicable to practical UXO field work. However, they demonstrate optimum discrimination ability and use a prototype instrument that provides an internally consistent basis for assessing the value of different combinations of spatial components and multiple time gates. The latter was implemented by decimating the data by component and channel to provide several alternative configurations acquiring one, two, or three spatial components and one or multiple time gates.

The seeded targets were divided into “ordnance-like” and “scrap-like;” the former were axisymmetric about a long axis whereas the latter were not. The triaxial time-dependent dipole model was used to estimate up to 18 parameters regarding target size, shape, position, and orientation. When nondimensionalized by the values along the object’s apparent longest axis, there are 8 parameters relevant to target size and shape. A generalized regression neural network was able to separate the ordnance-like items with a 91% true positive and 5% false-positive rate using the full multicomponent, multichannel data set. However, this was largely due to the larger sizes of the ordnance-like items compared to the scrap-like objects: the voltage decay approximately follows the $-3/2$ log-log slope that is theoretically expected for larger targets that are able to extend “intermediate time” through the measured time range. Further work on objects of comparable volume but different shape is necessary to determine whether the scrap-like objects still move through intermediate time more quickly because they generally have one very thin dimension. An alternative metric for the power-law slope that depends solely on axisymmetry—without regard to size—still yielded good discrimination: 32% false-positives at 91% true positives in the ordnance-like objects.

Multiple spatial components and multiple time channels were typically able reduce the false-positive rate by 40% or more over multiple-component, single-channel or single-component, multiple-channel decimated data sets, demonstrating the improved value of such systems for UXO discrimination.

6. REFERENCES

- Barrow, B.J., and Nelson, H.H, 1999, Model-based characterization of EM induction signatures for UXO/clutter discrimination using the MTADS Platform: *UXO Forum 99*, Dept. of Defense Explosives Safety Board, Alexandria, VA, CD-ROM.
- Barrow, B., and Nelson, H.H., 2001, Model-based characterization of EM induction signatures obtained with the MTADS electromagnetic array: *IEEE Transactions on Geosciences and Remote Sensing*, 39, 1279-1285.
- Bell, T., Barrow, B., and Miller, J.T., 2000, Subsurface discrimination using electromagnetic Induction Sensors: *IEEE Transactions on Geosciences and Remote Sensing*, 39, 1286-1293.
- Collins, L.M., Zhang, Y., Li, J., Jing, Wang, H., Carin, L., Hart, S.J., Rose-Pehrsson, S.L., Nelson, H.H., and McDonald, 2001, J.R., A comparison of the performance of statistical and fuzzy algorithms for unexploded ordnance detection: *IEEE Transactions on Fuzzy Systems*, 9, 17-30.
- Das, Y., McFee, J.E., and Stuart, G.C., 1990, Analysis of an electromagnetic induction detector for real-time location of buried objects: *IEEE Transactions on Geosciences and Remote Sensing*, 28, 278-287.
- Geonics, Ltd., 1996, EM61-3D Three Component Time Domain Electromagnetic UXO Detector Operating Notes (Preliminary): Mississauga, Ontario, Canada, 7 pp.
- Grant, F.S, and West, G.F., 1965, *Interpretation Theory in Applied Geophysics*: McGraw-Hill, New York, 584 pp.
- Grimm, R.E., Blohm, M., and E.M. Lively, 1997, UXO characterization using multicomponent, multichannel time-domain electromagnetic induction: *UXO Forum 97*, Dept. of Defense Explosives Safety Board, Alexandria, VA, 134-143.
- Grimm, R.E., and Sprott, T.A., 2002, Model-based sensor design optimization for UXO classification: *UXO/Countermine Forum 2002*, Dept. of Defense Explosives Safety Board, Alexandria, VA, CD-ROM.
- Hart, S.J., Shaffer, R.E., Rose-Pehrsson, S.L., and McDonald, J.R., 2000, Using physics-based modeler outputs to train probabilistic neural networks for unexploded ordnance (UXO) classification in magnetometry surveys: *IEEE Transactions on Geosciences and Remote Sensing*, 39, 797-804.
- Kaufman, A.A., and G.V. Keller, 1985, *Inductive Mining Prospecting Part 1: Theory*: Elsevier, Amsterdam, 620 pp.

- MacInnes, S.C., Snyder, D.D., and Zonge, K.L., 2002, Physics-based characterization of UXO from multicomponent TEM data, *UXO/Countermine Forum 2002*, Dept. of Defense Explosives Safety Board, Alexandria, VA, CD-ROM.
- McNeil, J.D., and Bosnar, M., 1996, Application of time domain electromagnetic techniques to UXO detection, *UXO Forum 96*, Dept. of Defense Explosives Safety Board, Alexandria, VA, pp. 34-42.
- Menke, W., 1984, *Geophysical Data Analysis: Discrete Inverse Theory*: Academic Press, Orlando, 260 pp.
- Nelson, H.H., McDonald, J.R., and Robertson, R., 2000, Design and construction of the NRL baseline ordnance classification test site at Blossom Point: *NRL/MR/6110-00-8437*.
- Pasion, L.R., and Oldenburg, D.W., 2001, A discrimination algorithm for UXO using time domain electromagnetics, *Journal of Environmental and Engineering Geophysics*, 6, 91-102.
- Wasserman, P.D., 1993, *Advanced Methods in Neural Computing*: Van Nostrand Reinhold, New York, 255 pp.
- Wold, R., Grimm, R., Tondra, M., Jander, A., George, D., and Becker, A., Detection and classification of UXO using multidimensional EM sensors, *UXO/Countermine Forum 2002*, Dept. of Defense Explosives Safety Board, Alexandria, VA, CD-ROM.